Cavities for light and sound: a cavity-enhanced platform for quantum acoustics

Fisicaro, M.

4 Observation of the optical Talbot effect from a surface acoustic wave dynamic grating

We demonstrate the dynamical Talbot effect caused by optical diffraction from standing surface acoustic waves. The Talbot effect is a wave interference phenomenon in the Fresnel regime, and we observe it by optically imaging 1 GHz (standing) surface acoustic waves with a fiber-based optical interferometer. By studying the interferometric signal at 1 GHz, we first discover the existence of an amplitude-modulated term, that can exceed in magnitude the usual phase-modulated term, enabling a new way of imaging surface acoustic waves. Secondly, we reveal with this method the Talbot effect, where a modified Talbot length appears. As a consequence, the amplitude modulation vanishes at periodic positions.

This chapter is based on M. Fisicaro, Y.C. Doedes, T. A. Steenbergen, M. P. van Exter and W. Löffler, Observation of the Talbot effect from a surface acoustic wave dynamic grating, arXiv:2409.11161 (submitted).

4.1 Introduction

The Talbot effect is a wave interference phenomenon in the Fresnel regime by diffraction of a plane wave by a periodic structure such as a grating. Upon diffraction of the wave by the grating, periodic images of the grating appear at specific distances; this phenomenon is also known as lensless imaging or self-imaging [109–111]. The Talbot effect was firstly discovered in optics in 1836 by Henry Fox Talbot [112], but it was Lord Rayleigh who quantitatively explained it in 1881 [113]. Four years later, Lord Rayleigh made another important scientific contribution by predicting the existence of a particular type of surface acoustic waves, characterized by an elliptical motion of the surface [1]. In his paper, he accurately predicted that these waves have a significant role in earthquakes and the collision of elastic solids, and they were later named Rayleigh waves in his honor. For about 140 years, these two physical phenomena have not been connected: despite the Talbot effect has been observed in many different systems [114–120], to the best of our knowledge, it has never been observed as a consequence of optical diffraction from Rayleigh waves.

In this study we demonstrate this phenomenon through optical imaging of standing Rayleigh waves, which, from now on, we will generically refer to as standing surface acoustic waves (SAWs).

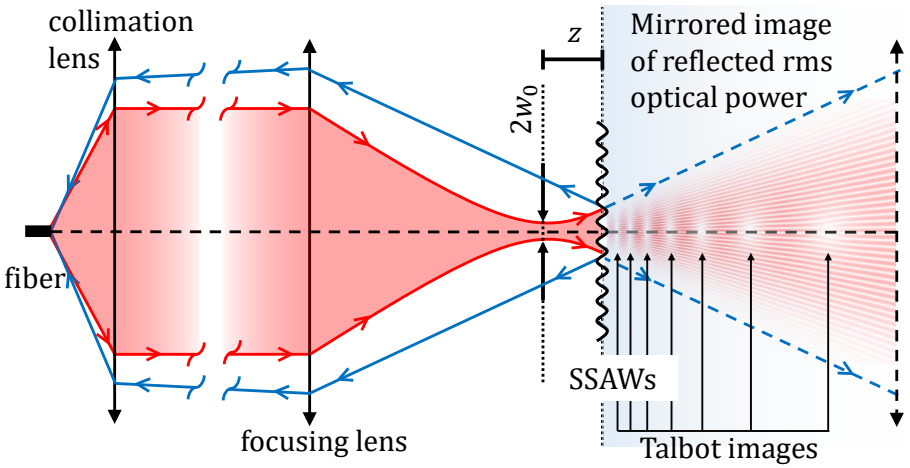

Figure 4.1: Sketch of the experiment: laser light from a single mode fiber is first collimated and then focused onto a partially reflecting surface on which standing surface acoustic waves (SSAWs) are excited. The incident light is reflected back, for clarity we plot here its mirrored image to the right of the reflecting surface. If the position of the beam waist z is displaced with respect to the reflecting surface, so that the light beam illuminates multiple periods of the oscillating surface grating, the Talbot effect can be observed where self-images of the field at the grating are reproduced in the near field at specific locations away from the grating. Here the self images are visible as regions of zero power on the right of the grating, where we have plotted the rms optical power of the reflected diffracted beam.

Surface acoustic waves (SAWs) can be excited using an interdigital transducer (IDT) [41,61,121] on the surface of a piezoelectric substrate at frequencies up to a few GHz, which for most materials corresponds to acoustic wavelengths down to the sub-micrometer range

[6,122–124]. If confined in an acoustic Fabry-Perot cavity [24,29,52,71–73,96,125] standing SAWs appear. This results in a surface that behaves as an oscillating surface grating, and can therefore dynamically diffract an optical beam upon reflection, by spatial phase modulation. In our case, we use a fiber-based scanning optical Michelson interferometer to image the displacement generated by 1 GHz SAWs. For spatially-resolved interferometric imaging of the SAWs, this diffraction is in principle an unwanted but unavoidable effect since at this frequency, the acoustic wavelength $\Lambda = 2.8\,\mu$m and the beam spot size of the focused laser beam $2w_0 = 2.8\,\mu$m (for $\lambda = 980\,$nm and 0.55 NA) are comparable in size.

In our experiment, we were originally interested in the optical phase modulation induced by the SAWs, but we found that the interferometric signal consists of both a phase modulation term, and of an amplitude modulation term that appears due to mode filtering by the single-mode optical fiber. In this paper, we theoretically and experimentally demonstrate that the amplitude modulation term is zero when the laser beam is precisely focused on the surface of the SAW device, due to the symmetry of the optical phase modulation with respect to the focal position of the laser beam. Additionally, this amplitude modulation term is also zero at periodic defocusing distances due to the interference between the directly reflected beam and the beams diffracted by the oscillating grating. This phenomenon can be better understood through the Talbot effect under Gaussian beam illumination.

When a grating is illuminated by a Gaussian beam, rather than a plane wave, the Talbot effect still occurs but with two notable differences (see Fig. 4.1) : first, the position of the self-images depends non-linearly on the distance z from the grating, and second, the self-images are magnified, with the magnification factor also varying non-linearly with z [126]. For each defocusing distance, the position and magnification of the self-images change, changing the Talbot pattern. Remarkably, we find that when the defocusing distance is an integer multiple of the usual Talbot length $z_T = 2\Lambda^2/\lambda$, the resulting Talbot patterns have a self-image located at the focal position of the fiber, leading to periodically spaced zeros in the amplitude modulation.

4.2 Experimental setup

The experimental setup shown in Fig. 4.2 (a) is a Michelson interferometer implemented with a polarization-mantaining single-mode fiber coupler as the beam splitter (PM BS). Narrow-linewidth laser light enters the fiber coupler through port A and is split into the sample (D) and reference arm (C). In the reference arm, the light is focused onto a mirror by a single aspheric lens and back-reflected into the fiber. In the sample arm (D), light is first collimated by an aspheric lens, and then strongly focused onto the GaAs-based SAW device with an aspheric lens with 0.55 NA, resulting in a beam waist radius $w_0 = 1.4\ \mu$m.

The GaAs surface acts as a partial mirror due to Fresnel reflection, and the reflected light is coupled back into the single-mode fiber using the same port D. The reflected light from the reference and sample arm of the interferometer is then recombined through the same fiber splitter, and exits through port B. For the SAW device, we nanofabricated on a GaAs substrate a surface acoustic wave (SAW) Fabry-Perot cavity, where surface acoustic waves are excited by an interdigital transducer (IDT) embedded inside the resonator (see inset in Fig. 4.2 (b)). In this way we can generate standing surface acoustic waves (SAWs) with a frequency of about 1 GHz, and a wavelength $\Lambda = 2.8\,\mu$m. These waves change the optical path length in the sample arm of the interferometer, generating an interferometric signal at 1 GHz which is detected with a fast photodiode.

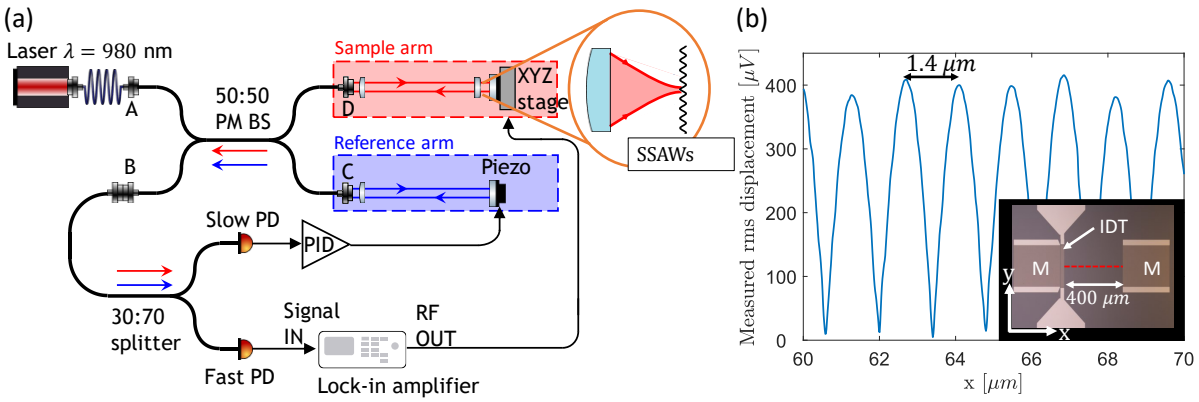

Figure 4.2: (a) Scheme of our experiment, a fiber-based Michelson interferometer using single-mode polarization-maintaining fibers, as described in the main text. (b) Microscope image (inset) of the SAW cavity showing the IDT and the SAW mirrors (M), and standing wave pattern measured along a short section of the dashed red line.

The interferometer is stabilized by a piezo actuator on which the mirror of the reference arm is mounted and a PID controller. The error signal is provided by the slow photodiode, and the PID controller is set to lock the interferometer to the side of an interference fringe. The SAW device is mounted on a three-axes nanopositioning stage, where translation along the optical (z) axis allows to adjust the focus of the laser beam, while the x and y axes allow us to scan the laser focus over the SAW device, in order to reconstruct an image of the out-of-plane displacement of the SAW device. Fig. 4.2 (b) shows a microscope image of the SAW device, and a cross-section along the x-direction of the standing acoustic waves, as indicated by the red line, with the laser focus exactly at the sample plane. Since we are plotting the rms amplitude of the measured displacement, the spatial periodicity is $\Lambda/2 = 1.4\,\mu m$.

This measurement was taken with a locked interferometer, but we have found that even if the reference arm of our interferometer is blocked, we can sometimes observe the SAW signal very clearly. This is because on top of the usual optical phase changes induced by the standing SAWs, the coupling to the single mode fiber (port D) also changes the optical power by spatial mode filtering of the reflected light, effectively converting phase changes induced by the SAW into changes of the optical power coupled back into the fiber. We refer to this effect as amplitude modulation. Thus, the measurement shown in Fig. 4.2 (b) can be taken even by only using the sample arm of the interferometer, and it shows the same periodicity but different amplitude. However, it is important to notice that for this to happen, we need to defocus the device from the laser focus, because exactly in the focus the 1 GHz amplitude modulation is zero, due to the equal symmetry of the standing SAWs and the optical phase around the beam focus. As we will show later, we also expect a very weak 2 GHz amplitude modulation, but we intentionally limit our detection bandwidth to around 1 GHz.

4.3 Amplitude and phase modulation

We now present an analytical model that describes the interferometric signal for the fiber-based Michelson interferometer. In particular we will show how the interferometric signal

is affected by the optical wavelength λ, the SAW wavelength Λ, and the Gaussian beam radius at the GaAs surface w. We will show analytically that the interferometric signal contains an amplitude modulation term that persists also when the reference arm of the interferometer is blocked. Finally we will compare the analytic results to our experimental data, and we will show how both are a consequence of the Talbot effect.

4.3.1 Complex collection ratio

With Fig. 4.2 (a) in mind, let us consider what happens in the sample arm of the interferometer: light from a single mode fiber is imaged and focused onto a reflecting SAW device. The reflected light follows the same path in reversed direction and is collected by the same fiber. The same happens in the reference arm, and the two beams coming from the two arms of the interferometer are then recombined in the fiber beam splitter and interfere at the fast photodiode, which measures the intensity of the light. The standing SAWs induce time-periodic variations of the local curvature of the reflected light, leading to 1 GHz modulation of the amplitude and phase of the light in the single-mode fiber. Importantly, we not only consider that the SAW device is in-focus, but discuss the generic case where the focus is at distance z from the SAW device. Since we use linearly polarized light and the fiber coupler is polarization maintaining, is is sufficient to use scalar fields for the input field E_{in}, the collected field E_{col}, and the reference field E_{ref}. We introduce the complex collection ratio

$$\alpha(t) \;=\; \frac{E_{col}(t)}{E_{in}}, \tag{4.1}$$

which is a measure of the amplitude and phase of the reflected light collected by the single mode fiber, relative to the input light that enters the sample arm of the interferometer. Once we know $\alpha(z,t)$, we can write the total intensity at the fast photodiode as

$$\begin{aligned} I_{tot} \;&=\; |E_{ref} \;+\; \alpha(t)\; E_{in}|^2 \\ &=\; I_{ref} \;+\; |\alpha(t)|^2 I_{in} \;+\; \mathrm{Re}[2\alpha(t) E_{in} E_{ref}^*], \end{aligned} \tag{4.2}$$

where Re denotes the real part. Due to the small amplitude of the excited surface acoustic waves (in our case 140 pm), we can neglect second-order loss contribution due to scattering into other spatial modes. We also note that while phase variations in $\alpha(t)$ are only visible in the double product term of Eq. 4.2, amplitude variations are also visible in the $|\alpha(t)|^2 I_{in}$ term and can be observed also with blocked reference arm when $E_{ref} = 0$.

The calculation of the complex collection ratio $\alpha(t)$ is based on the overlap integral between the Gaussian mode supported by the fiber and the beam reflected by the SAW device, as a function of the defocusing, namely the distance z between the SAW device surface and the beam waist position of the focused Gaussian beam. This overlap integral can be calculated at any plane, for simplicity we choose to calculate it on the device surface, so that we don't have to compute how the electric field propagates after reflection. Due to the presence of standing SAWs along the x axis, we can model the surface out-of-plane displacement as

$$\Delta d(x,y,t) \;=\; A(t)\;\cos\left[K\,(x - x_0)\right]\;, \tag{4.3}$$

where $K = 2\pi/\Lambda$ is the SAW wave number, x_0 is the transverse distance between the center of the laser focus and the position of the standing SAW anti-node, and $A(t) = A_0\cos(\Omega t)$, is the time-dependent amplitude of the SAW with angular frequency Ω and

peak displacement A_0. There is no dependency on y because the standing SAW are excited only along the x axis. In Eq. 4.1, we defined the complex collection ratio as a function of time, but now we compute it also as a function of z and x_0: $\alpha(t) \rightarrow \alpha(z, x_0, t)$. From calculations shown in the Appendix 4.5.1 we obtain:

$$\begin{aligned} \alpha(z, x_0, t) &= \alpha_{DC}(z) + \alpha_{AC}(z, x_0)\cos(\Omega t) \\ \alpha_{DC}(z) &= \frac{1}{1 + i\tilde{z}} \\ \alpha_{AC}(z, x_0) &= \frac{2ikA_0\cos(Kx_0) \times \exp\left[-B\left(1 - i\tilde{z}\right)\right]}{1 + i\tilde{z}} \end{aligned} \tag{4.4}$$

Here, $\tilde{z} = z/z_R$, $z_R = \pi w_0^2/\lambda$ is the Rayleigh range of the focused Gaussian beam, w_0 its waist radius, $k = 2\pi/\lambda$ the wavenumber, and $B = K^2 w_0^2/8$. The complex collection ratio $\alpha(z, x_0, t)$ can be separated in two parts: a static term $\alpha_{DC}(z)$ which is a Lorentzian function of z and describes the complex collection ratio in the absence of standing SAWs, and a dynamic term $\alpha_{AC}(z, x_0)$, which describes the effect of the time modulation of the light field by the standing SAWs. This dynamic term not only contains the Lorentzian attenuation as a function of the defocusing, but also an additional exponential term that depends on the ratio between the Gaussian waist radius w_0 and the acoustic wavelength Λ via B. This exponential is a complex number, meaning that $\alpha_{AC}(z, t)$ has a certain periodicity in z. In the next section we will provide an explanation of this periodicity by using the Talbot effect.

4.3.2 Single-beam experiment: amplitude modulation

Here we block the reference arm, so that the signal is only given by the amplitude modulation. The quantity responsible for the amplitude modulation is $|\alpha(z, x_0, t)|^2$, and as shown in Appendix 4.5.1, $|\alpha(z, x_0, t)|^2 = |\alpha(z)|^2_{DC} + |\alpha(z, x_0)|^2_{\Omega}\cos(\Omega t) + |\alpha(z, x_0)|^2_{2\Omega}\cos(2\Omega t)$. In our experiment we are only interested in the Ω component since the AC coupled RF photodiode blocks the DC component, and the lock-in amplifier demodulates at Ω. Moreover, the 2Ω term is much smaller in amplitude than the Ω term, since it scales like A_0^2, as opposed to A_0 for the Ω term. After the demodulation by the lock-in amplifier, we are left with an rms signal of the amplitude modulation given by:

$$V_{amp}^{rms}(z) \propto \frac{2|\gamma|e^{-B}}{\sqrt{2}(1 + \tilde{z}^2)} \times |\sin(B\tilde{z})| \ , \tag{4.5}$$

where $\gamma = 2kA_0\cos(Kx_0)$ and the proportionality symbol means that we are not taking into account the gain provided by photodiode and lock-in amplifier. This equation gives periodic zeros at positions that solve the equation $\sin(B\tilde{z}) = 0$, and substituting $B = K^2 w_0^2/8 = \pi^2 w_0^2/(2\Lambda^2)$ and $\tilde{z} = z\lambda/(\pi w_0^2)$, we find that the positions of the zeros is given by z=$n \times z_T$, where n is an integer, and $z_T = 2\Lambda^2/\lambda$ is the classical Talbot length for a diffraction grating with period Λ, illuminated by a plane wave.

4.3.3 Two-beams experiment: phase modulation

Here we interfere light from the sample arm with light from the reference arm. From Eq. 4.2, we see that the phase modulation is detected via $2\mathrm{Re}\left[\alpha(z, x_0, t)E_{in}E_{ref}^*\right]$, where

$E_{ref} = E_{in} \times \exp(i\phi_{ref})$ and in the experiment, we adjust the intensity in the reference arm of the interferometer to be equal to the DC intensity in the sample arm at zero defocusing: $|\alpha(z = 0)|^2_{DC} = 1$. We stabilize the interferometer by locking ϕ_{ref} to a specific value of optical intensity I_{lock} via the feedback loop controlling the piezo in the reference arm. In our case we lock at the side of a fringe, which means $\phi_{ref} = \pm\pi/2$ and $I_{lock} = 2I_{ref}$, but only at $z = 0$. In our measurements we vary the distance z between the beam focus and the SAW device, therefore α_{DC} changes both in amplitude and phase, causing ϕ_{ref} to change in order to keep the interferometer locked at the same optical power. While we can calculate $\phi_{ref}(z)$ from Eq. 4.2, imposing that $I_{tot} = I_{lock}$, a more useful quantity is the difference between the phase of $\alpha_{DC}(z)$, and the phase of the reference beam $\Delta\phi(z) = \arg[\alpha_{DC}(z)] - \phi_{ref}(z)$:

$$\Delta\phi(z) \simeq \mp \operatorname{acos}\left[\frac{\sqrt{1+\tilde{z}^2}}{2}\left(\frac{\mathrm{I_{lock}}}{\mathrm{I_{ref}}} - 1 - \frac{1}{1+\tilde{z}^2}\right)\right], \tag{4.6}$$

where the sign is chosen whether we lock the interferometer on a positive $(-)$ or negative $(+)$ slope. We note that in the derivation of this equation we considered $\arg(\alpha_{DC}) \simeq \arg(\alpha)_{DC}$, and $|\alpha_{DC}| \simeq |\alpha|_{DC}$, which is allowed since the SAW displacement is very small. The rms of the total interferometric signal is obtained by calculating the rms value of the Ω component of Eq. 4.2, which for small SAW displacement A_0 can be approximated as:

$$V^{rms}_{tot} \simeq \frac{2\,|\gamma|\,e^{-B}}{\sqrt{2}}\left|\frac{\sin(\Delta\phi + B\tilde{z})}{\sqrt{1+\tilde{z}^2}} + \frac{\sin(B\tilde{z})}{1+\tilde{z}^2}\right|. \tag{4.7}$$

The first term in the modulus is from the phase modulation, while the second term originates from amplitude modulation. In detection, the phase modulation term can not be separated from the amplitude modulation term, as it is the result of interference. In mathematical terms, $V^{rms}_{tot} \neq V^{rms}_{amp} + V^{rms}_{phase}$ due to the non-linearity of the modulus function.

4.3.4 Comparison to experiments

Now we compare our theory to experiments where we measure both the amplitude modulation V^{rms}_{amp} and the total interferometric signal V^{rms}_{tot} as a function of the defocusing z, distance between the beam focus and SAW device. In particular, we show the results corresponding to the situation where the focused Gaussian beam is centered on an antinode of the standing SAW, corresponding to $x_0 = 0$ in Eqs. 4.5 and 4.7. While changing the defocusing z, the relative position x_0 between the antinode and the beamspot could change due to imperfect alignment, we do a short line scan along the x direction, exemplarily shown in Fig. 4.2 (b), and we average the amplitudes of the measured peak values.

In Fig. 4.3 (a) we show the measured $|\alpha_{DC}|^2$ as a function of z, corresponding to the DC light intensity coupled back to the fiber in the sample arm of the interferometer measured with the slow photodiode (see Fig. 4.2 (a)), reproducing the expected Lorentzian dependency. Fig. 4.3 (b) shows the measured amplitude modulation V^{rms}_{amp} in blue, as well as the total interferometric signals V^{rms}_{tot}, obtained by locking the interferometer on the positive (red) or negative (yellow) slope on the side of the fringe. The measured signal is the rms Voltage detected by the lock-in amplifier after 1 GHz demodulation, and the grey areas are regions where it is not possible to lock the interferometer at the side of the fringe due to a decrease in the light intensity coupled back to the fiber in the sample

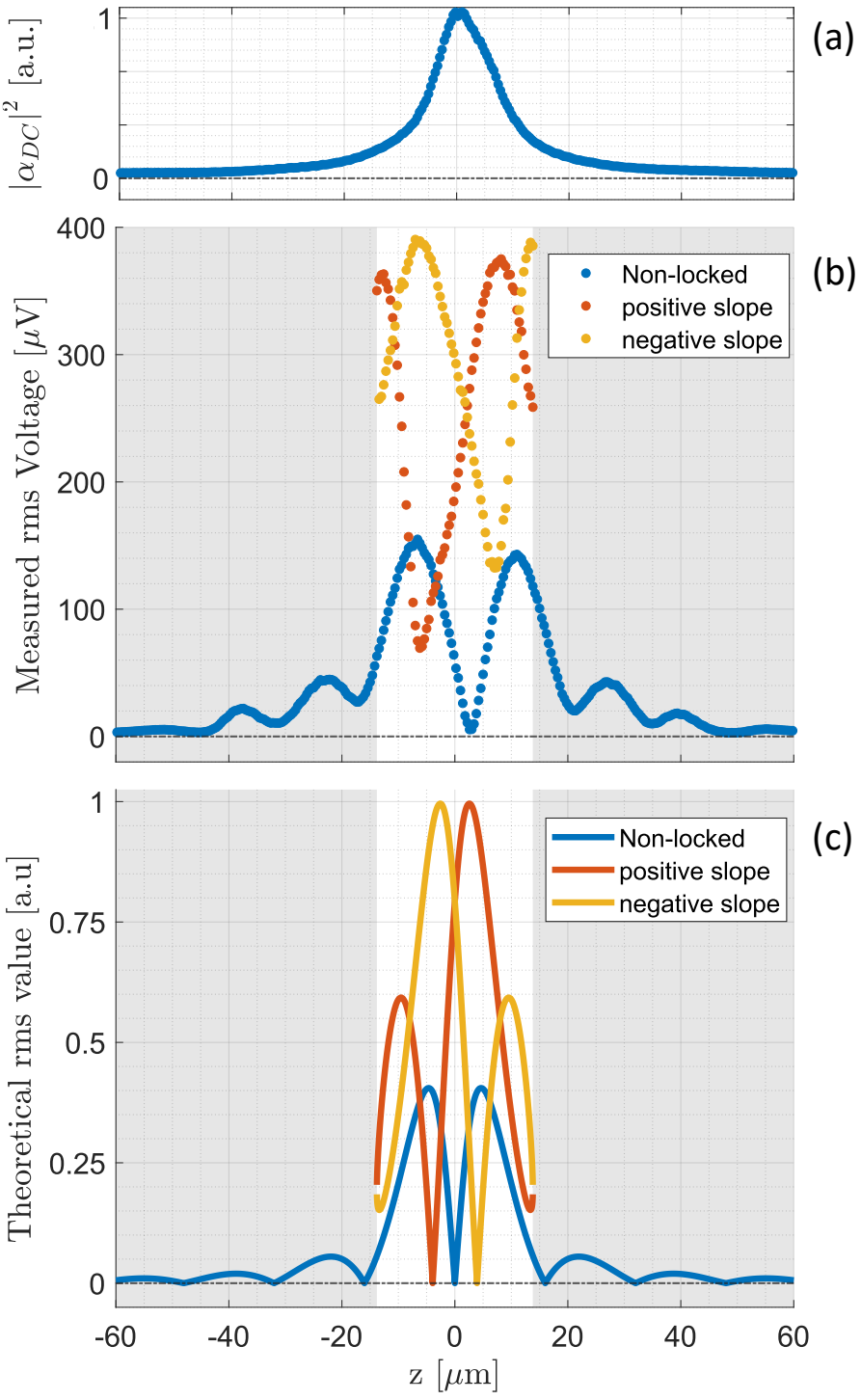

Figure 4.3: (a) Experimental DC component of the complex collection ratio as a function of the defocusing z. (b) Experimental and (c) theoretical Ω component of the amplitude modulation (blue) and of the total interferometric signals for the interferometer locked at the positive (red) or negative (yellow) slope of the fringe.

arm of the interferometer. Fig. 4.3 (c) shows the corresponding theoretical data based on Eqs. 4.5, 4.6 and 4.7.

We observe excellent qualitative agreement between measurements and theory: the signals are almost symmetric with respect to the z defocusing, the total interferometric signals locked at a positive and negative slope intersect at the defocusing z for which the amplitude modulation is zero, and the positions of the minima in the amplitude modulation are close-to-periodic with period $z_{period} = (15.6 \pm 2.8)\,\mu$m, where the error is the standard error. This value is quite close to the expected periodicity from Eq. 4.5: $z_T = 2\Lambda^2/\lambda = 16\,\mu$m.

Residual misalignment of the sample arm of the interferometer can explain the few quantitative differences we observe, such as the minimum of the amplitude modulation located at $z \simeq 3\,\mu$m instead of $z = 0$, and the asymmetry in the height of the peaks between negative and positive detunings, both in the amplitude modulation and in the total interferometric signals. Spurious reflections inside the fiber beam splitter are most likely the reason why the measured signals don't reach zero, except for the central dip in the amplitude modulation.

4.3.5 Explaining the periodicity: the Talbot effect

We have seen from Eq. 4.5 that the amplitude modulation is a signal periodic in z with the period $z_T = 2\Lambda^2/\lambda$. In an attempt to find an intuitive explanation for this phenomenon, we will now show that this is a consequence of the optical Talbot effect caused by diffraction of the laser beam from the standing SAWs. If a reflective grating with periodicity Λ is illuminated by a plane wave under normal incidence, on top of the directly reflected plane wave (zero order), there are diffracted plane waves at angles $\theta \simeq \pm p\,\lambda/\Lambda$ ($\sin(\theta) \simeq \theta$ for $\lambda << \Lambda$), where p is a positive integer corresponding to the diffraction order. In the near field, interference of all the diffracted fields creates periodic replicas of the light field at the grating at integer multiples of the Talbot length $z_T = 2\Lambda^2/\lambda$.

We start with a standing SAW grating described by Eq. 4.3 for $x_0 = 0$ and $t = 0$, where the peak displacement of the standing SAWs is maximum. On the optical axis, we define a new coordinate system $\overline{z}$, with the SAW device placed at the origin $\overline{z} = 0$, and the beam focus at position $\overline{z} = z$. For clarity, we unfold the back reflected light propagation to the right of $\overline{z} = 0$, as shown in Fig. 4.4. In this new coordinate system, and due to the symmetric unfolding with respect to $\overline{z} = 0$, the projected image of the fiber is always at position $\overline{z} = -z$, and the field coupled back to the fiber after reflection, is the field at this position, after mode-matching to the fiber.

Since we know the optical field at the grating plane $\overline{z} = 0$, we can propagate it to any other plane using the Fresnel-Kirchhoff diffraction integral, and in particular we can calculate the transverse field at $\overline{z} = -z$. A detailed calculation is shown in Appendix 4.5.2, but in Fig. 4.4 (a) we plot an example of the computed diffraction integral at many planes, showing the intensity of the propagated light field after reflection from the grating.

We report here the most important results of the calculation: due to the small SAW displacement, only the first diffraction orders are present, corresponding to two beams tilted at angles of $\theta = \pm\lambda/\Lambda$ with respect to the optical axis. Interference of the zero order and the first-order beams creates periodic images of the field at the grating. Contrary to the case of a grating illuminated by a plane wave, under Gaussian beam illumination, these self-images are laterally magnified by a factor $M_G = R_{\overline{z}}/(R_{\overline{z}} - \overline{z})$ [126], where $R_{\overline{z}} = (\overline{z} - z) \times (1 + z_R^2/(\overline{z} - z)^2)$ is the radius of curvature of the Gaussian beam at a

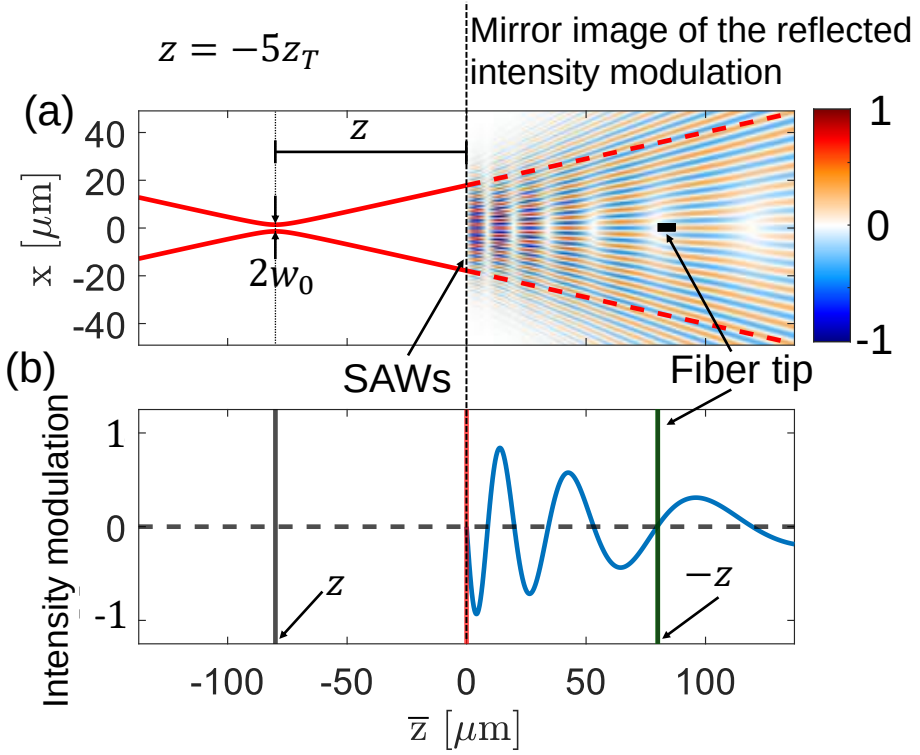

Figure 4.4: Example of Talbot pattern obtained with a beam defocusing of $z = -5z_T$. (a) shows for $\overline{z} < 0$ the Gaussian beam before the grating , and for $\overline{z} > 0$ the mirrored image of the reflected light intensity modulation, with respect to the constant intensity of the non-diffracted Gaussian beam. We considered a SAW profile given by Eq. 4.3 , for $x_0 = 0$ and $t = 0$. Self-images of the field at the grating appear at specific positions given by Eq. 4.8, where here are visible as zones with zero intensity modulation . (b) shows a cross-sectional plot of (a) along $x = 0$, showing that on the optical axis, the intensity modulation of the reflected field is zero at the positions of the self-images, and in particular at the mirrored position of the image of the fiber tip as indicated.

generic observation plane $\overline{z}$. As shown in Ref. [126] the positions of these self images, also non-periodic in $\overline{z}$, are given by solving

$$m\frac{z_T}{2} = \frac{R_{\overline{z}} - \overline{z}}{R_{\overline{z}}} \times \overline{z} \,, \tag{4.8}$$

where m is a positive integer. From this equation it is clear that depending on the distance z between the beam focus and the SAW grating, the radius of curvature $R_{\overline{z}}$ changes, and with it, also the Talbot pattern created after reflection.

Each of these different Talbot patterns have self-images at different positions, obtained by solving Eq. 4.8 but, remarkably, we find in Appendix 4.5.2 that when the beam focus is at the distances $z = n \times z_T$ from the grating, with n an integer number, there is always one of the self-images at the position $\overline{z} = -z$, coinciding with the position of the projected image of the fiber.

This is visible in Fig. 4.4 (a) where for $\overline{z} \geqslant 0$ we show the intensity modulation, relative to the intensity of a non-diffracted Gaussian beam, as well as a cross section of this field along the optical axis $x = 0$ (b). These plots show the intensity of the diffracted light field at time $t = 0$, with respect to the intensity of a non-diffracted Gaussian beam (without

SAWs). After half period of the SAW oscillation, at time $t = T/2$, the plots are the same with the only difference that positive (red) and negative (blue) intensity fluctuations are exchanged.

The intensity of the field at the positions of the self-images is constant in time, because the reflection from SAWs acts as a phase grating, therefore modulating only the phase of the light field, as visible by writing the field at the grating, after reflection:

$$\psi^{-}_{reflect}(\overline{z} = 0, x, t) \;=\; \psi^{+}_{in}(\overline{z} = z) \times \exp\left[2ikA_0 \cos(Kx)\cos(\Omega t)\right] \;. \tag{4.9}$$

In Fig. 4.4 (a), we can also observe that the region of constant intensities are concentrated close to the optical axis ($x = 0$)- this is because we are illuminating only a small portion of the grating. We note that also the number of self-images obtained after reflection depends on the Gaussian beam radius at the grating, and therefore on the number of grating periods that are illuminated. In particular, the minimum beam radius needed to observe a number m of self-images is given by (derivation in Appendix 4.5.2):

$$w_{min}(m) \;=\; \Lambda\sqrt{\frac{2m}{\pi}} \;. \tag{4.10}$$

Despite the intensity of the field at the positions of the self-images is time independent, in principle this is not enough to ensure that the amplitude modulation is zero at the positions of the self-images, because mode-matching to the fiber can convert the time-dependent phase with angular frequency Ω, into a time-dependent amplitude of the field with the same angular frequency. However at the positions of the self images, this does not happen, as shown in the calculation for the complex collection ratio.

Although we did not find a truly intuitive explanation for this effect, we provide here a heuristic picture; first we consider the case where the laser beam is focused on the SAW device: at the surface, the wavefront of the non-diffracted Gaussian beam is flat, which correspond to a constant phase on the xy plane. The reflected Gaussian beam at the SAW surface is given by Eq. 4.9 for $z = 0$, and we can see that the corresponding surface displacements at the times $t = 0$, and time $t = T/2$, corresponding to half oscillation period, are symmetric with respect to the flat wavefront of the non-diffracted Gaussian beam. Because of this, the amplitude of the field mode-matched to the fiber is the same at the times $t = 0$ and $t = T/2$, giving rise to the 2Ω modulation as shown in Appendix 4.5.1, and no Ω component.

Now we consider the case where the laser beam is defocused with respect to the SAW device, specifically being at a distance $z = n \times z_T$ such that the projected image of the fiber is at the position of the $n-$th Talbot image. While at this position the amplitude of the field is time independent, because it is an image of the amplitude of the field at the SAW grating, the phase is not time independent. Moreover, in this case, the non-diffracted Gaussian beam has a finite radius of curvature, leading to a non-constant phase on the xy plane: the surface displacement over one oscillation period is not symmetric anymore with respect to the phase of the non-diffracted Gaussian beam. However, given the small spatial extension of the fiber along the xy plane, the radius of curvature of the no-diffracted Gaussian beam can be approximated as flat. The result is that once again, the amplitude of the field coupled back to the fiber, has only 2Ω modulation, and no Ω modulation. Despite this picture is a simplification and does not fully grasp the complexity of the real experiment, it can be a useful tool to understand the phenomenon, without having to explicitly calculate the overlap integral between the field supported by the fiber and the propagated field after diffraction from the SAW grating.

4.4 Conclusions and outlook

By using a fiber-based Michelson interferometer to measure GHz standing SAWs in a SAW cavity, we discovered that on top of the usual phase modulation term, the total interferometric signal also has a significant amplitude modulation term. We measured the strength of the amplitude modulation as a function of the probe beam defocusing, and showed that the amplitude modulation vanishes at zero defocusing, but also at periodic defocusings from the SAW device, corresponding to multiples of the Talbot length. This is surprising as for non-plane wave illumination, Talbot self-images usually appear at non-periodic distances [126]; while this is true, the positions of the self-images change as we change the beam defocusing, but we find that when the beam defocusing is a multiple of the Talbot length, there is always a self-image created at the projected image of the collecting fiber.

We want to point out here that our experiment shows that an interferometric setup is not always the optimal solution for measuring spatially-resolved oscillating surface displacements such as induced by SAWs, and simple amplitude measurements in a single-mode fiber-coupled setup can be an easier way. Then, the fiber splitter can be replaced by a fiber circulator which maximizes the optical power available at the oscillating surface, and therefore maximizing the measured signal. Depending on the SAW period Λ and the beam waist radius w_0, the amplitude modulation can even be stronger than the conventional interferometric signal – if $\Lambda \lesssim w_0$.

4.5 Appendix

4.5.1 The complex collection ratio

Here we derive the complex collection ratio $\alpha(z, x_0, t)$. We use the shifted reference frame where the focus of the Gaussian beam, as projected image of the input fiber, is the origin of the optical axis, and the reflecting surface is at a distance z. This shift does not change the final results that depend only on the relative distance between the SAW device and the focus of the Gaussian beam. We consider the ideal case where the imaging system produces a perfect image of the fiber tip in the focus. This field can be written as $E_{in}(x, y, z, t) = \psi^+_{in}(x, y, z) \exp(-ikz + i\omega t)$ with a forward-propagating Gaussian mode (without Gouy phase)

$$\begin{aligned} \psi^+_{in}(x, y, z) &= \frac{\sqrt{2}}{\sqrt{\pi} w(z)} \times \exp\left[-ik \frac{x^2 + y^2}{2q(z)}\right] \\ &= \frac{\sqrt{2}}{\sqrt{\pi} w(z)} \times \exp\left[-\frac{x^2 + y^2}{w^2(z)}(1 + i\tilde{z})\right], \end{aligned} \tag{4.11}$$

where $q(z) = z + iz_R$ is the complex beam parameter, $z_R = \pi w_0^2/\lambda$ is the Rayleigh range, w_0 is the beam waist radius located at $z = 0$, $w(z) = w_0\sqrt{1 + \tilde{z}^2}$ is the beam radius at position z, and $\tilde{z} = z/z_R$. The field is normalized:

$$\iint |\psi^+_{in}(x, y, z)|^2 \, dx \, dy = 1. \tag{4.12}$$

The complex collection ratio defined in the main text can be calculated via the overlap integral between the reflected backward-propagating field, and the backward-propagating image of the input field $\psi^-_{in} = (\psi^+_{in})^*$. This overlap integral can be calculated at any z plane, since optical propagation is a unitary operation. We calculate it at the plane of the SAW device. For a flat and perfectly reflecting interface, the reflected field mimics the input field $E^-_{refl} = E_{in}$, and we obtain the DC coupling:

$$\alpha_{DC} = \iint \psi^+_{in}(x, y, z)^2 \, dx \, dy = \frac{1}{1 + i\tilde{z}} .$$

We can calculate the in-coupling efficiency η as

$$\eta = |\alpha_{DC}|^2 = \frac{I_{col}}{I_{in}} = \frac{1}{1 + \tilde{z}^2} , \tag{4.13}$$

which corresponds to the DC coupling when we displace the reflecting surface by an amount z, with respect to the position of the beam waist.

We now consider how standing surface acoustic waves (SAWs) modulate the complex collection ratio α. In presence of standing SAWs, the reflecting surface oscillates with profile

$$\Delta z(x, y) = A(t) \cos[K(x - x_0)], \tag{4.14}$$

where $K = 2\pi/\Lambda$ is the SAW wave number, Λ is the SAW wavelength, $A(t) = A_0 \cos(\Omega t)$ is the displacement at an anti-node with amplitude A_0, Ω is the SAW angular frequency, and x_0 indicates the position of the laser beam. The reflected field becomes

$$\psi^{-}_{refl} = \exp(2ik(z+\Delta z)\psi^{+}_{in} \ , \tag{4.15}$$

where $\Delta z > 0$ is away from the input fiber. From Eq. 4.15, we remove the stationary phase factor $\exp(2ikz)$, and we obtain

$$\alpha(z, x_0, t) = \iint \exp(2ik\Delta z)\psi^{+}(x, y, z)^2 \ dx \ dy. \tag{4.16}$$

Substituting 4.14 into 4.16, we arrive at the following integral:

$$\begin{aligned} \alpha(z, x_0, t) \ &= \ \iint \exp\{2ikA(t)\cos[K(x-x_0)]\} \\ &\times \ \exp\left[-\frac{2(x^2+y^2)(1+i\tilde{z})}{w^2(z)}\right] \ \frac{dx \ dy}{\pi w^2(z)} \ . \end{aligned} \tag{4.17}$$

This integral can be solved by separating the integral in x and y direction:

$$\begin{aligned} \alpha(z, x_0, t) \ &= \ \frac{2}{\pi w^2(z)} \ I_y \ I_x \ , \ \text{where} \\ I_y \ &= \ \int_{-\infty}^{+\infty} \exp\left[-\frac{2y^2}{w^2(z)}(1+i\tilde{z})\right] \ dy \\ I_x \ &= \ \int_{-\infty}^{+\infty} \exp\left[-\frac{2x^2}{w^2(z)}(1+i\tilde{z})\right] \ \times e^{2ik\Delta z} \ dx. \end{aligned} \tag{4.18}$$

I_x and I_y can be solved by using the standard integral

$$\int_{-\infty}^{+\infty} \exp\left[-ax^2+ibx\right] \ dx \ = \ \sqrt{\frac{\pi}{a}} \exp\left(-\frac{b^2}{4a}\right) \ . \tag{4.19}$$

While evaluation of I_y is straightforward, yielding

$$I_y = \sqrt{\frac{\pi}{2(1+i\tilde{z})}} w(z) \ , \tag{4.20}$$

evaluating I_x requires a few more steps: first we separate the generic standing SAW displacement in Eq. 4.14 into the sine and cosine quadratures:

$$\cos\left[K(x-x_0)\right] \ = \ \cos(Kx)\cos(Kx_0) + \sin(Kx)\sin(Kx_0) \ , \tag{4.21}$$

then, since $kA(t) << 1$, we can expand the exponential:

$$\begin{aligned} \exp\{2ikA(t)\cos[K(x-x_0)] \ &\simeq \\ 1 + 2ikA(t)[\cos(Kx)\cos(Kx_0) + \sin(Kx)\sin(Kx_0)] \ . \end{aligned} \tag{4.22}$$

Multiplication of this term by the Gaussian function, and their integration, leads to I_x. We observe that, since $\sin(Kx)$ is an odd function of x, whereas the Gaussian function is even, the integral vanishes and we obtain:

$$I_x = I_y + 2ikA(t)\cos(Kx_0) \times \int_{-\infty}^{+\infty} \exp\left[-\frac{2x^2}{w^2(z)}(1+i\tilde{z})\right]\cos(Kx)\,dx\ . \tag{4.23}$$

We can use the expansion $\cos[Kx] = [\exp(iKx) + \exp(-iKx)]/2$ to obtain the following equation:

$$I_x = I_y + ikA(t)\cos(Kx_0) \times (G^+ + G^-),\ \text{where} \tag{4.24}$$
$$G^{\pm} = \int_{-\infty}^{+\infty} \exp\left[-\frac{2x^2}{w^2(z)}(1+i\tilde{z})\right] \times \exp(\pm iKx)\ dx.$$

The physical meaning of this equation is the following: for a small SAW displacement A_0, the reflecting surface behaves as an amplitude diffraction grating with cosine profile. The Gaussian beam impinges on this diffraction grating, and the back reflection is coupled back to the fiber (term I_y in Eq. 4.24) . The diffraction grating also generates two tilted Gaussian beams with angles $\theta^{\pm} = \pm\lambda/\Lambda$, corresponding to the terms G^+ and G^- in Eq. 4.24, as will be shown in Appendix 4.5.2. By using once again the standard integral 4.19, we obtain:

$$G^{\pm} = \sqrt{\frac{\pi}{2(1+i\tilde{z})}}w(z)\exp\left[-B(1-i\tilde{z})\right]\ , \tag{4.25}$$

where $B = -K^2w_0^2/8$. Inserting Eq.4.25 into I_x, and I_x into Eq. 4.18, we get:

$$\alpha(z, x_0, t) = \frac{1}{1+i\tilde{z}}\left\{1 + 2ikA(t)\cos(Kx_0)\exp\left[-B(1-i\tilde{z})\right]\right\}\ . \tag{4.26}$$

The amplitude modulation term is given by $|\alpha(z,t)|^2$, which after some calculations can be expressed as:

$$\begin{aligned} |\alpha|^2 &= |\alpha|^2_{DC} + |\alpha|^2_{\Omega}\cos(\Omega t) + |\alpha|^2_{2\Omega}\cos(2\Omega t) \\ |\alpha|^2_{DC} &\simeq \frac{1}{1+\tilde{z}^2} \\ |\alpha|^2_{\Omega} &= -\frac{2\gamma \times \exp(-B) \times \sin(B\tilde{z})}{1+\tilde{z}^2} \\ |\alpha|^2_{2\Omega} &= \frac{\gamma^2 \times \exp(-2B)}{2(1+\tilde{z}^2)}\ , \end{aligned} \tag{4.27}$$

where $\gamma = 2kA_0\cos(Kx_0)$.

4.5.2 The Talbot effect

Here we explicitly calculate the propagated field after the grating, used to create the plots in Figs. 4.1 and 4.4, and to visualize the Talbot patterns created by diffraction of a Gaussian beam from a periodic grating. Since the grating affects the propagated field only along the x transverse direction, for simplicity we study the evolution of a 1D Gaussian beam after reflection from the surface.

On the optical axis, we define a new coordinate system $\overline{z}$ with the origin at the surface of the SAW device. In this coordinate system, the beam focus is at position $\overline{z} = z$, where z is the beam defocusing introduced in the calculations for the complex collection ratio. For clarity, and as illustrated in Fig. 4.4 in the main text, we unfold the reflected field to the right of $\overline{z} = 0$. The field at the surface ($\overline{z} = 0$) is given by the function

$$\psi^{-}_{reflect}(\overline{z} = 0, x, t) = \psi^{+}_{in}(z) \times \exp\left[2ikA(t)\cos(Kx_0)\cos(Kx)\right] \ ,$$

where we omitted the sine quadrature in the expansion of the displacement (Eqs. 4.14, 4.22) due to integration in the next step. The field $g(x, \overline{z}, t)$ at a generic position $\overline{z}$ is given by convolution of the input field $\psi^{-}_{reflect}(\overline{z} = 0, x, t)$ with the impulse response function of free space in the Fresnel approximation (Fresnel-Kirchhoff diffraction integral):

$$h(x, \overline{z}) \simeq h_0 \exp\left(-i\frac{\pi}{\lambda\overline{z}}x^2\right) \ , \tag{4.28}$$

where $h_0 = i/(\lambda\overline{z})$, leading to

$$g(x, \overline{z}, t) = h_0 \int_{-\infty}^{+\infty} \psi^{-}_{reflect}(x', t) \times \exp\left[-i\frac{\pi}{\lambda\overline{z}}\left(x - x'\right)^2\right] \ dx' \ . \tag{4.29}$$

Following the same steps we used to calculate the complex collection ratio $\alpha(z, t)$, we expand the exponential containing the cosine term:

$$\begin{aligned} &\exp\left[2ikA(t)\cos(Kx_0)\cos(Kx)\right] \simeq 1 + i\gamma(t)\cos(Kx), \\ &\text{where } \gamma(t) = 2kA_0\cos(Kx_0)\cos(\Omega t) \ . \end{aligned} \tag{4.30}$$

Physically this means that for small SAW displacements, the phase grating described above can be approximated by an amplitude grating with cosine profile, and a phase shift of $\pi/2$ given by the imaginary number in front of the cosine. We can expand the cosine in exponential form: $\cos(Kx) = \left[\exp(iKx) + \exp(-iKx)\right]/2$, and finally we can rewrite Eq. 4.29 as

$$\begin{aligned} g(x, \overline{z}, t) = &\int_{-\infty}^{+\infty} \psi^{+}_{in} \times h(x - x', \overline{z}) \ dx' \\ &+ \frac{i\gamma(t)}{2} \int_{-\infty}^{+\infty} \psi^{+}_{in} \times \exp(iKx') \times h(x - x', \overline{z}) \ dx' \\ &+ \frac{i\gamma(t)}{2} \int_{-\infty}^{+\infty} \psi^{+}_{in} \times \exp\left(-iKx'\right) \times h(x - x', \overline{z}) \ dx' \ . \end{aligned} \tag{4.31}$$

The first term describes the evolution of a Gaussian beam, and therefore represents the backreflected Gaussian beam, as if it was reflected from a flat surface. The second and third terms describe two tilted beams at an angle of $\theta = \pm\lambda/\Lambda$ with respect to the optical axis, as we can see by writing the second (+) and third (-) terms as:

$$\begin{aligned} g_{\pm} = \frac{i\gamma(t)h_0 C}{2} \exp\left(-\frac{i\pi x^2}{\lambda\overline{z}}\right) &\int_{-\infty}^{+\infty} \exp\left[-ax'^2\right] \\ &\times \exp\left[ix'\frac{2\pi}{\lambda\overline{z}}\left(x \pm \overline{z}\frac{\lambda}{\Lambda}\right)\right] \ dx' \ , \end{aligned} \tag{4.32}$$

where

$$a = \left(\frac{1 + iz/z_R}{2w_0^2(1 - z^2/z_R^2)} + \frac{i\pi}{\lambda \overline{z}} \right) , \tag{4.33}$$

and C is a normalization factor. The integral in Eq. 4.31 can be solved by using the standard integral from Eq. 4.19. We do not show here the lengthy expression, but an example solution is shown in Fig. 4.4 in the main text, where we evaluated the integral at $t = 0$ and $z_0 = 5z_T$.

As a result of the interference between the diffracted beams, self-images of the field at the grating appear at non-periodic positions on the optical axis. These positions are dependent on the radius of curvature of the field impinging on the grating, and therefore on the beam defocusing z. Therefore different values of z, leads to different Talbot patterns.

4.5.2.1 Existence and positions of the self images

Here we solve Eq. 4.8, and we show that for beam defocusings $z = nz_T$, where n is an integer, one of the self-images is always located at $\overline{z} \simeq -z$, which in our coordinate system and with the unfolded reflection, corresponds to the position of the projection of the image of the fiber. We will also give a proof for Eq. 4.10.

Starting by substitution of $R_{\overline{z}} = (\overline{z} - z)(1 + z_R^2/(\overline{z} - z)^2)$ into Eq. 4.8, we obtain a second order equation $a\overline{z}^2 + b\overline{z} + c = 0$,where $a = z + mz_T/2$, $b = -(mzz_T + z^2 + z_R^2)$, $c = mz_T(z^2 + z_R^2)/2$. This equation has two solutions given by

$$\overline{z}_{1,2} \;=\; \frac{m\ z\ z_T + z^2 + z_R^2 \pm (z^2 + z_R^2)\sqrt{1 - \delta^2}}{2(z + mz_T/2)} , \tag{4.34}$$

where $\delta \;=\; mz_T z_R/(z^2 + z_R^2)$. The first thing we notice is that the solutions only exist if $\delta^2 \leq 1$, which, under the condition that $m > 0$, leads to the equation:

$$z_0^2 \;\geq\; z_R\ (m\ z_T - z_R) , \tag{4.35}$$

which gives the minimum distance between the beam waist of the focused Gaussian beam and the grating, in order to observe a number m self images. This equation can be rewritten in terms of the beam radius at the grating, showing that in order to see m self-images, the minimum beam radius at the grating has to be

$$w_{min}(m) \;=\; \Lambda \sqrt{\frac{2m}{\pi}} . \tag{4.36}$$

We can now see what happens to Eq. 4.34 when $z \;=\; nz_T$, in the limit that $\delta \ll 1$, where we can approximate $\sqrt{1 - \delta^2} \simeq 1$:

$$\overline{z}_{1,2} \;\simeq \frac{m\ n\ z_T^2 + n^2 z_T^2 + z_R^2 \pm (n^2 z_T^2 + z_R^2)}{z_T(2n + m)} , \tag{4.37}$$

and by choosing the solution with the (-) sign, we obtain $\overline{z}_1 \;\simeq z_T \times mn/(2n + m)$, and for $n = -m$ we get $\overline{z}_1 = -nz_T$, proving that the n-th self image lies at the position $\overline{z} \simeq -z$. To check if $\delta << 1$, we can introduce a variable a equal to the ratio between the SAW wavelength and the beam waist radius, such that $\Lambda = aw_0$, and we can write

$$\delta \;=\; \frac{2\pi\ m\ a^2}{\pi^2 + 4\ m^2 a^4} . \tag{4.38}$$

We can see that $\delta \sim m^{-1}$ when $m \to \infty$, therefore the approximation is better for high values of m. In our experiment $a = 2$ ($\Lambda = 2.8\ \mu m$ and $w_0 = 1.4\ \mu m$), and already for $m = 1$,the approximation used in Eq. 4.37 is valid.